RESEARCH ARTICLE
SPACE PHYSICS: MAGNETOSPHERIC PHYSICS

Earth and Planetary Physics
8: 247–257, 2024
doi: 10.26464/epp2023051

Background removal from global auroral images: Data-driven dayglow modeling

A. Ohma*, M. Madelaire, K. M. Laundal, J. P. Reistad, S. M. Hatch, S. Gasparini, and S. J. Walker

Birkeland Centre for Space Science, Department of Physics and Technology, University of Bergen, Bergen, Norway

Key Points:

- We present a data-driven dayglow model for global auroral images.
- The method uses robust statistics and automatically deselects auroral pixels.
- The method allows for slow temporal variations.

Citation: Ohma, A., Madelaire, M., Laundal, K. M., Reistad, J. P., Hatch, S. M., Gasparini, S., and Walker, S. J. (2024). Background removal from global auroral images: Data-driven dayglow modeling. *Earth Planet. Phys.*, *8*(1), 247–257. http://doi.org/10.26464/epp2023051

Abstract: Global images of auroras obtained by cameras on spacecraft are a key tool for studying the near-Earth environment. However, the cameras are sensitive not only to auroral emissions produced by precipitating particles, but also to dayglow emissions produced by photoelectrons induced by sunlight. Nightglow emissions and scattered sunlight can contribute to the background signal. To fully utilize such images in space science, background contamination must be removed to isolate the auroral signal. Here we outline a data-driven approach to modeling the background intensity in multiple images by formulating linear inverse problems based on B-splines and spherical harmonics. The approach is robust, flexible, and iteratively deselects outliers, such as auroral emissions. The final model is smooth across the terminator and accounts for slow temporal variations and large-scale asymmetries in the dayglow. We demonstrate the model by using the three far ultraviolet cameras on the Imager for Magnetopause-to-Aurora Global Exploration (IMAGE) mission. The method can be applied to historical missions and is relevant for upcoming missions, such as the Solar wind Magnetosphere Ionosphere Link Explorer (SMILE) mission.

Keywords: aurora; dayglow modeling; global auroral images; far ultraviolet images; dayglow removal

1. Introduction

Global auroral cameras are key tools used in revealing the complex interplay between the magnetized solar wind and Earth. Whereas in situ instruments on satellites provide high-precision measurements from a localized region, remote sensing provides large-scale measurements of the state and evolution of the coupled magnetosphere–ionosphere system.

The first images of the aurora taken from space were obtained by the Isis-2 scanning photometer, which sampled large fractions of the polar region in visible wavelengths during each orbit (Anger et al., 1973; Lui et al., 1975). Before this, the full auroral oval could only be examined statistically by combining numerous ground-based observations from limited regions (e.g., Vestine, 1944; Feldstein, 1964). With the KYOKKO aurora observation satellite came the first camera in the far ultraviolet (FUV) range, enabling measurements also in the sunlit hemisphere (Kaneda et al., 1977; Hirao and Itoh, 1978). The first truly global images were obtained by the Dynamics Explorer 1 (DE-1) mission (Frank et al., 1981). It had the entire oval within the field of view for up to 5 hours, which provided direct observations of how the polar cap expands and contracts as the magnetospheric system responds to external solar wind forcing (Frank and Craven, 1988). Since then, Viking (Anger et al., 1987), Akebono (Oguti et al., 1990), Polar (Acuña et al., 1995; Frank et al., 1995; Torr et al., 1995), Interball-2 (Zelenyi et al., 1997), and Imager for Magnetopause-to-Aurora Global Exploration (IMAGE; Burch, 2000; Mende et al., 2000) spacecraft have provided large-scale images of the aurora with temporal resolutions on the order of seconds or minutes from high Earth orbits. In addition to these high-altitude imagers, several satellites in low Earth orbits have been able to scan the aurora in different wavelengths, providing one image per orbit with high spatial resolution.

These imagers have greatly improved our knowledge of the auroral morphology and dynamics, and have revealed distinct auroral features in the main oval (e.g., Cogger et al., 1977), equatorward of the oval (e.g., Anger et al., 1978; Elphinstone et al., 1993; Burch et al., 2002; Immel et al., 2002), and in the polar cap (e.g., Frank et al., 1981, 1986; Murphree et al., 1990; Frey et al., 2003a; Zhang QH et al., 2021). Because of the strong coupling to the magnetosphere, auroral observations have been used to examine meso-scale structures in the magnetotail (Sergeev et al., 2000; Zesta et al., 2000) and asymmetries in the magnetospheric system (Østgaard et al., 2003, 2011, 2018; Laundal and Østgaard, 2009;

Correspondence to: A. Ohma, anders.ohma@uib.no
Received 29 NOV 2022; Accepted 11 APR 2023.
First Published online 26 JUN 2023.
©2023 by Earth and Planetary Physics.

Ohma et al., 2018). Auroral imagers also provide quantitative measurements of the characteristic energy and energy flux of precipitating particles, and from these the ionospheric conductance (Kamide et al., 1986; Lummerzheim et al., 1991; Germany et al., 1994a; b; Frey et al., 2003b). While incoherent scatter radars (in particular) or particle measurements from spacecraft can provide these quantities with higher certainty, the strength of global cameras lies in their ability to provide instantaneous estimates over a large region with good spatial and temporal resolution (Brekke et al., 1993).

Large-scale FUV images of the aurora are thus a key tool in space physics. There are, however, two main sources of ionospheric FUV emissions observed from space: precipitating particles (which produce the aurora) and photoelectrons produced by sunlight. The sunlight-induced dayglow is most intense at the subsolar point, and it decreases as the solar zenith angle α_s increases. The intensity of the dayglow also depends on the flux of the extreme ultraviolet (EUV) solar radiation and on the atmospheric composition, which affects both the production and absorption of dayglow (Meier, 1991). The solar radio flux at 10.7 cm ($F_{10.7}$) is usually used as a proxy of the EUV flux. In addition to dayglow, nightglow emissions and scattered sunlight from the atmosphere contribute to the background signal in specific wavelengths. The angle at which the emissions are observed, α_d, also affects the measured intensities; if emission lines that are optically thin (not absorbed by the atmosphere) are observed at an angle, the effective volume of the emission region is larger compared to observations from the nadir, causing a stronger observed signal.

It is often necessary to remove all non-auroral emissions from the images when analyzing the auroral component. Many auroral phenomena appear in the sunlit hemisphere, and fair comparison of the extent and intensity of auroral features between different locations or at different times can only be done if the full background is removed. The same applies to statistical considerations and quantitative estimations based on FUV images, which warrant the need for robust background modeling. The dayglow intensity can be modeled from first principles (Strickland et al., 1999) or empirically via observations. Liou et al. (1997) binned Polar data from the Ultraviolet Imager (UVI) below 60° magnetic latitude on α_s and fitted a cosine function to make a smooth background model. Wang LM et al. (2018) fitted $A\cos^2(P\alpha_s)$ to individual images while ignoring emissions at typical auroral latitudes, and then used hourly averages of A and P to construct a model that depends on $F_{10.7}$, universal time, and day of year. Nicholas et al. (1997) made an empirical background model for DE-1 by binning 178 images obtained during magnetically quiet periods by both α_s and α_d and then fitting a surface to the binned data. A similar approach has been applied to the Global Ultraviolet Imager (Paxton et al., 1999; Christensen et al., 2003) and the Special Sensor Ultraviolet Spectrographic Imager (Paxton et al., 1992) in low Earth orbit (Zhang Y and Paxton, 2008; Zhang YL et al., 2022): A reference model is constructed by using quiet time passes while considering both the solar zenith angle and look angle of each pixel. This reference model is then scaled to individual passes by minimizing the misfit to the observed emissions, thus accounting for variations in dayglow intensity caused by, for example, variations in solar radiance.

While Earth's dayglow is mainly aligned with the solar zenith angle, it is also affected by atmospheric conditions. During geomagnetically active periods, heating of the upper atmosphere leads to upwelling of N_2 and O_2, and a subsequent depletion of atomic O. This depletion is not symmetric around noon, but is most pronounced at dawn (Craven et al., 1994). This causes dawn–dusk asymmetries in the dayglow. For this particular reason, Immel et al. (2000) included two extra angular dependencies in their empirical model of DE-1 images in addition to α_s and α_d: a phase angle orthogonal to the solar zenith angle and an azimuthal angle relative to the subsolar longitude. This allowed their model to also capture asymmetries in the background emissions.

While the aforementioned methods make models from a collection of images, background emissions can also be modeled for each image individually. Lummerzheim et al. (1997) used only nadir-looking images and binned each image by the solar zenith angle. They then calculated the mean intensity in each bin while ignoring emissions from auroral latitudes, and subtracted these mean values from the original image to get a background-corrected image. Reistad et al. (2013, 2014, 2016) followed a similar approach but binned the intensities in each pixel by $\cos\alpha_s/\cos\alpha_d$ to account for the viewing geometry and used the binned median instead of the mean. Li X et al. (2004) fitted the function $A + B\cos\alpha_s + C\cos\alpha_d$ to Polar UVI images, and Laundal and Østgaard (2009) and Laundal et al. (2010b) fitted a two-dimensional polynomial to IMAGE and Polar FUV images while ignoring emissions from auroral latitudes. The background intensity has also been determined regionally by dividing images in circular sectors around the magnetic pole and then fitting a Gaussian/double Gaussian (intended to represent the aurora) plus a second-order polynomial (non-aurora) to the latitudinal intensity profiles to find the boundaries of the oval (Carbary et al., 2003; Laundal et al., 2010a; Longden et al., 2010).

In this paper, we demonstrate a data-driven approach to modeling non-auroral emissions in global FUV images by using robust statistics while allowing temporal variations in the background model. The method can be applied to historical missions and is relevant for upcoming missions, such as the Solar wind Magnetosphere Ionosphere Link Explorer (SMILE) mission (Raab et al., 2016). To demonstrate the model, we use data from the three FUV imagers on IMAGE. The data are introduced in the next section. We describe the approach in Section 3 and discuss the benefits and limitations of the proposed method in Section 4. The Python code to use this method and the data set used in this publication are publicly available (Ohma et al., 2022a, 2022b).

2. Data

We use global images obtained by the FUV cameras (Mende et al., 2000a) on board the Imager for IMAGE mission (Burch, 2000), which was operational from 2000 to 2005. IMAGE had a spin period of about 123 s, and auroral images were obtained once during each spin period when the detectors scanned the Earth. Three cameras in the FUV range monitored the aurora: the Wideband Imaging Camera (WIC), which was sensitive to emissions in the Lyman–Birge–Hopfield (LBH) range (Mende et al., 2000b), and two spectographic imagers (Mende et al., 2000c), one sensitive to the Doppler shifted 121.8 nm hydrogen line (hereafter SI12) and one sensitive to the 135.6 nm oxygen line (hereafter SI13). The WIC had an integration time of 10 s, whereas SI12 and SI13 had an integration time of 5 s. To illustrate the method, we use data from one orbit, spanning from 07:24 to 16:38 on 28 August 2000. Figure 1 shows images obtained at 09:40:57 using the three cameras.

The raw images obtained by the cameras are corrected to account for temperature and voltage differences throughout the lifetime of IMAGE. A part of this processing is a flat-field correction, which takes into account sensitivity differences in the direction parallel to the spin axis of IMAGE (vertical direction in Figure 1). The images have the highest sensitivity near the center and weaker sensitivity at the top and bottom. The values of the flat-field correction *FF* were found by examining the response of each camera to dayglow at middle latitudes when IMAGE was near perigee (Frey et al., 2003b). The intensities I_0 of all images are then scaled by *FF* to produce a corrected intensity *I*. However, I_0 consist not only of the real signal I_s that the detector was exposed to, but also a constant noise level *C*. The original scaling is therefore

$$I(r,c) = FF(r) \cdot I_0(r,c) = FF(r) \cdot [I_s(r,c) + C], \tag{1}$$

where *r* and *c* are the row and column of the detector as oriented in Figure 1.

Figure 2a displays the WIC image in Figure 1a with the original flat-field correction applied. The color map is highly saturated to highlight the background. There are clear intensity differences across the detector in the vertical direction unrelated to aurora or dayglow. This difference is also seen in the upper right part of the image, which illustrates background space with no emissions. It is thus clear that the flat-field correction is not working perfectly. However, simply omitting the correction causes a significant increase in the spread in regions with a real signal (dayglow and aurora). The flat-field correction is thus necessary, but we believe that it should not be applied to the static background noise in WIC, only to the signal. To fix this issue, we assume that *C* is constant across the image and take the median of all pixels with a solar zenith angle larger that 100 (dark hemisphere) or pixels not pointing at the Earth to determine its value. We then remove the noise before we apply *FF*, such that

$$I(r,c) = FF(r) \cdot \Big[I_0(r,c) - C\Big] + C = FF(r) \cdot I_s(r,c) + C. \tag{2}$$

We have chosen to add *C* after the flat-field correction to keep the intensities similar to the original implementation, but this is not strictly necessary. The result is shown in Figure 2b, indicating a clear improvement of the intensity difference across the detector. This change is applied only to WIC, as we have not seen indications

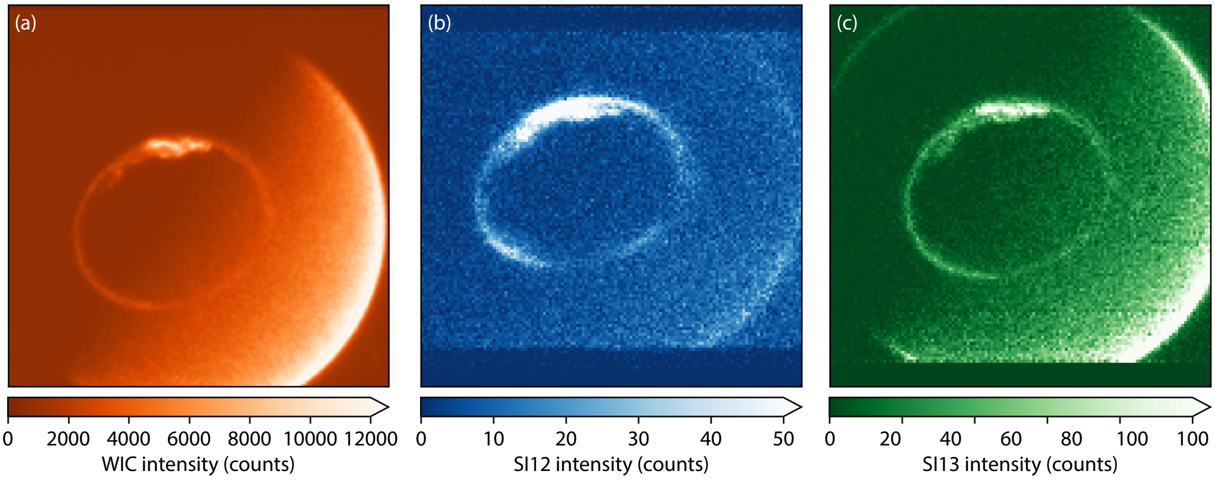

Figure 1. Global far ultraviolet images from (a) WIC, (b) SI12, and (c) SI13 of the northern hemisphere aurora at 09:40:57 on 28 August 2000.

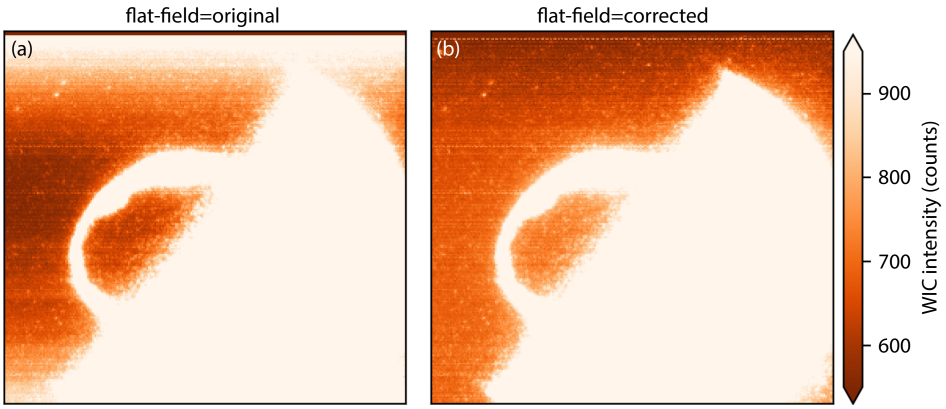

Figure 2. WIC image obtained on 28 August 2000 at 09:40:57 with (a) the original flat-field implementation and (b) the corrected flat-field implementation.

of similar problems in the two other detectors, probably because C is small in those cameras.

3. Background Removal

In this section, we describe a data-driven model that solves for the non-auroral background counts in the time period spanned by the input FUV images. We first describe how we model the part of the dayglow aligned with the solar zenith angle while also accounting for the viewing angle, which models most of the background signature. We then describe how we model large-scale residuals and typically asymmetric background.

3.1 B-spline Model

The modeling scheme described here is a development of the method proposed by Ohma et al. (2018). First, we note that the intensity I of emissions in the FUV range approximately follows $I = I_0 \cos\alpha_s$ when seen from the nadir, where α_s is the solar zenith angle. Second, we take into account that the pixels in the detector generally observe the ionosphere at an angle. The dayglow emission lines considered in this study are all optically thin. The entire height segment h where the emissions are produced thus contribute to the observed signal. When the emissions are observed at an angle, the effective height of this emission column increases as $h^* = h/\cos\alpha_d$. Here, α_d refers to the viewing angle of the observation. On the basis of these arguments, we choose to model I as a function of $x = \cos\alpha_s/\cos\alpha_d$.

Figure 3a displays the observed WIC intensities from 09:38:55, 09:40:57, and 09:43:00 UT on 28 August 2000 versus x. There is a near constant background for $x < 0$ (nightside), intense emissions near $x = 0$ (aurora), and a monotonically increasing trend for $x > 0$ (dayside). The dayglow intensity can be modeled as a spline function, which again can be expressed as a linear combination of B-splines (cf. de Boor, 2001),

$$I_{\mathrm{bs}}(\alpha_s, \alpha_d, t) = \sum_{n=1}^{N} a_n(t)\, B_n(\cos\alpha_s/\cos\alpha_d), \tag{3}$$

where a_n is the magnitude of the corresponding B-spline B_n. As described below, the temporal dependence is modeled by using a separate set of B-splines. We therefore refer to the B-splines in Equation (3) as spatial B-splines. Each of these spatial B-splines is non-zero at an interval along x specified by the degree and knot locations used. The spatial B-splines used to model I_{bs} are displayed in Figure 3b, and are of order 3 with dense knot locations (vertical red lines) around zero to accommodate the fast transition of I_{bs} across the terminator. In addition, there are exterior knots at

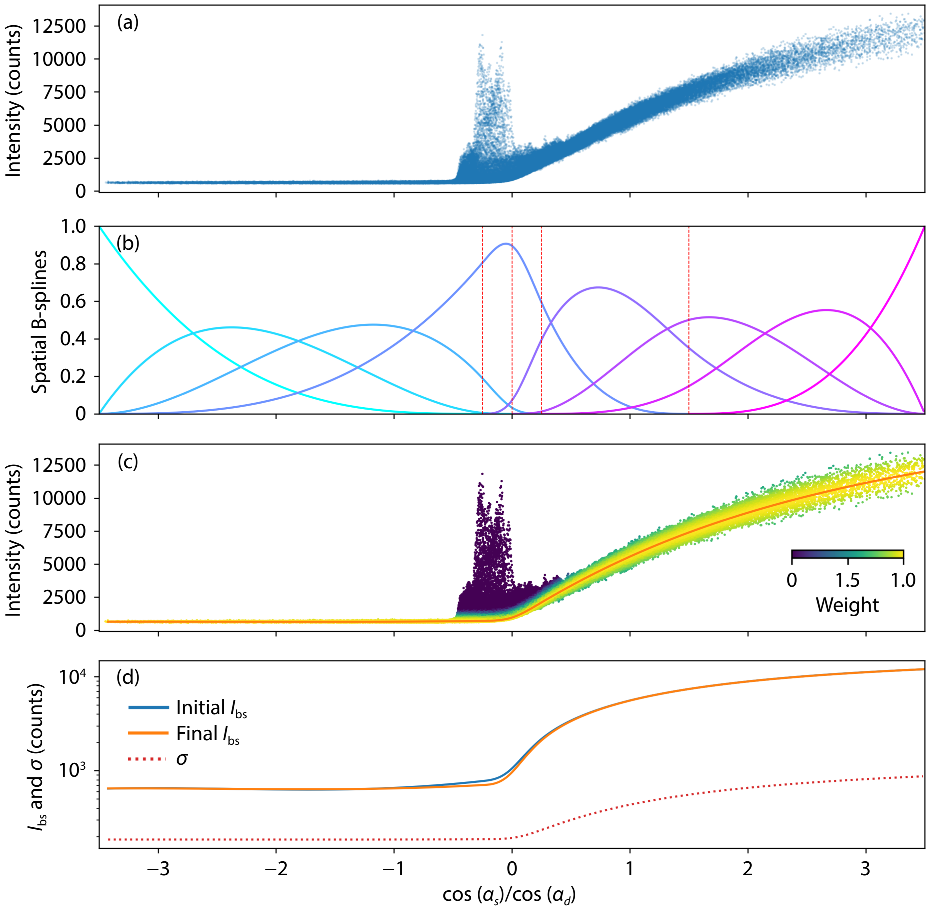

Figure 3. (a) Observed WIC intensities at 09:38:55, 09:40:57, and 09:43:00 on 28 August 2000 sorted by $x = \cos\alpha_s/\cos\alpha_d$. (b) Spatial B-spline functions used to model the background. The vertical red lines indicate the locations of interior knot points. (c) Background model (orange) and the weight of the WIC observations in Figure 3a after the final iteration. (d) Modeled background intensity I_{bs} (solid) for the first (blue) and final (orange) iteration on a logarithmic scale. The dashed line shows σ.

the two end points.

Figure 4a displays the temporal evolution of the observed WIC intensities during the entire orbit, where the binned mean intensity along x is in the vertical direction. Constant values for $x < 0$ and monotonically increasing values with increasing x for $x > 0$ are seen at all time steps, but there are clear variations in the intensity. There are rapid jumps between subsequent images, in addition to a general reduction of the observed intensity at the dayside from the beginning to the end of the event. As there can be temporal variations in the dayglow intensity, it is beneficial to have a model that allows for slow variations in the modeled intensity. Ohma et al. (2018) took this into account by allowing the spatial B-spline coefficients to vary linearly in time. Here we instead use temporal B-splines, which allows for a much more flexible model. To do this, we rewrite Equation (3) as

$$I_{\mathrm{bs}}(\alpha_s, \alpha_d, t) = \sum_{l=1}^{L}\sum_{n=1}^{N} a_{nl}\, B_n\left(\cos\alpha_s/\cos\alpha_d\right) B_l\left(t\right), \tag{4}$$

where the coefficients a_{nl} are the magnitude of the B-splines $B_n\left(\cos\alpha_s/\cos\alpha_d\right)$ and $B_l(t)$. If temporal knots are located only at the first and last time step of an interval, a temporal order of zero yields a constant dayglow model. An order of one yields a linear time variation, an order of two a quadratic time variation, and so on. Knots can also be placed within the modeled time interval, allowing even finer temporal fitting. We note that the model will be smooth in time only for a temporal order of two or greater if there are knots within the considered time interval; otherwise the model will be discontinuous (order zero) or have infinite gradients (order one) at the knots. In this study, we have used temporal B-splines of order two with an approximate 140-min knot separation (evenly spaced knots between the first and last time step in the event) as displayed in Figure 4b. The locations of the interior knots are indicated by the vertical red lines.

The goal is to obtain the model coefficients a_{nl} that best describe the background at any given time. We write the forward problem as

$$\boldsymbol{d} = \boldsymbol{G}_{\mathrm{bs}}\boldsymbol{m}_{\mathrm{bs}}, \tag{5}$$

where $\boldsymbol{d}$ is a column vector with the observed intensities and $\boldsymbol{m}_{\mathrm{bs}}$ is a column vector containing the model coefficients a_{nl}. The matrix $\boldsymbol{G}_{\mathrm{bs}}$ describes the linear relationship between $\boldsymbol{d}$ and $\boldsymbol{m}_{\mathrm{bs}}$ given by Equation (4), commonly referred to as the design matrix. We use a combination of iterative reweighting and zeroth-order Tikhonov regularization to reduce the influence of auroral emissions and avoid overfitting. We thus model $\boldsymbol{m}_{\mathrm{bs}}$ as the least-squares solution of

$$\boldsymbol{m}_{\mathrm{bs}} = \left(\boldsymbol{G}_{\mathrm{bs}}^{\mathrm{T}}\boldsymbol{W}\boldsymbol{G}_{\mathrm{bs}} + \lambda^2\boldsymbol{I}\right)^{-1}\boldsymbol{G}_{\mathrm{bs}}^{\mathrm{T}}\boldsymbol{W}\boldsymbol{d}. \tag{6}$$

The regularization parameter λ determines the trade-off between minimizing data misfit and the model norm, and $\boldsymbol{I}$ is the identity matrix. The diagonal matrix $\boldsymbol{W}$ represents the weight of each observation and is decomposed into $\boldsymbol{W} = \boldsymbol{W}_c\boldsymbol{W}_t$. The diagonal matrix $\boldsymbol{W}_c$ contains weights related to data coverage to reduce spatial bias, defined as the inverse of the number of measurements in equal bins along x at each time step. The diagonal matrix $\boldsymbol{W}_t$ contains weights that are updated iteratively to reduce the influence of outliers such as aurora. We use Tukey weights (Beaton and Tukey, 1974), where the weight of each measurement k is defined as

$$w_k = \begin{cases} \left[1 - \left(\dfrac{e_k}{c\sigma_k}\right)^2\right]^2 & , \quad |e_k| \le c\sigma_k. \\ 0 & , \quad |e_k| > c\sigma_k. \end{cases} \tag{7}$$

Here, e_k is the misfit given by $d_k - I_{\mathrm{bs},k}$, σ_k is the spread of the observations, and c is a scaling factor we have set to 5. It is common to use a single value for σ_k, often the root mean square error (RMSE). However, the noise in our model is clearly heteroskedastic along x. To accommodate this, we first calculate the RMSE in bins; a single bin for $x < 0$ and 15 bins for $0 \le x < 3.5$. We use all the images in the event and assume that the noise is constant with respect to time. To find a continuous noise model, we assume that total variance σ^2 is proportional to I_{bs}^2, such that

$$\sigma^2 = s_d^2 I_{\mathrm{bs}}^2 + \sigma_d^2, \tag{8}$$

where s_d^2 and σ_d^2 represent the relative and absolute variance of the detector. The two coefficients s_d^2 and σ_d^2 are found as the least-squares solution when putting the binned RMSE on the left side of this equation. We then get a smooth estimate of the variance by inserting the two parameters into Equation (8), which is subsequently used in Equation (7).

Tukey weights set outliers to zero. We believe that this is more appropriate than weighting schemes that only reduce the importance of outliers, such as the commonly applied Huber weights (Huber, 1964), as the main outliers in the background model are not observational extremes but rather observations of a different distribution (aurora) than the one we are trying to model (dayglow). The model is updated iteratively until the relative change of the 2-norm of $\boldsymbol{m}_{\mathrm{dg}}$ between two iterations is less that 0.001. The regularization parameter λ is found by using a standard L-curve analysis (Hansen, 1992). For the time interval considered in this study, reasonable values for λ are 0.01, 0.1, and 0.1 for WIC, SI12, and SI13 images, respectively. When the final $\boldsymbol{m}_{\mathrm{bs}}$ is determined, we get the modeled dayglow intensity by using Equation (4).

The performance of the B-spline (BS) model is displayed in Figures 3c, 3d, 4c, 4d, and 5. Figure 3c shows the final BS model in orange together with the observed intensities. The color of each point represents its weight after the final iteration. Here we see that the auroral pixels have been down-weighted and that the noise acceptance is greater at the dayside compared to the nightside. Figure 3d displays I_{bs} on a logarithmic scale for the initial (blue) and final (orange) iterations. Here we see the effect of the iterative scheme; the background is initially overestimated near $x = 0$ because of the aurora, but this effect is reduced as the auroral observations are down-weighted. In Figure 4c we see the temporal evolution of the background model, which clearly captures the gradual change shown in Figure 4a. Figure 4d displays how the final model coefficients a_{1l} (cyan) to a_{Nl} (pink) vary in time. This is thus the temporal evolution of the magnitude of the spatial B-splines in Figure 3b.

Finally, Figure 5 shows the BS model applied to the images obtained at 09:40:57 on 28 August 2000. From the top, the rows

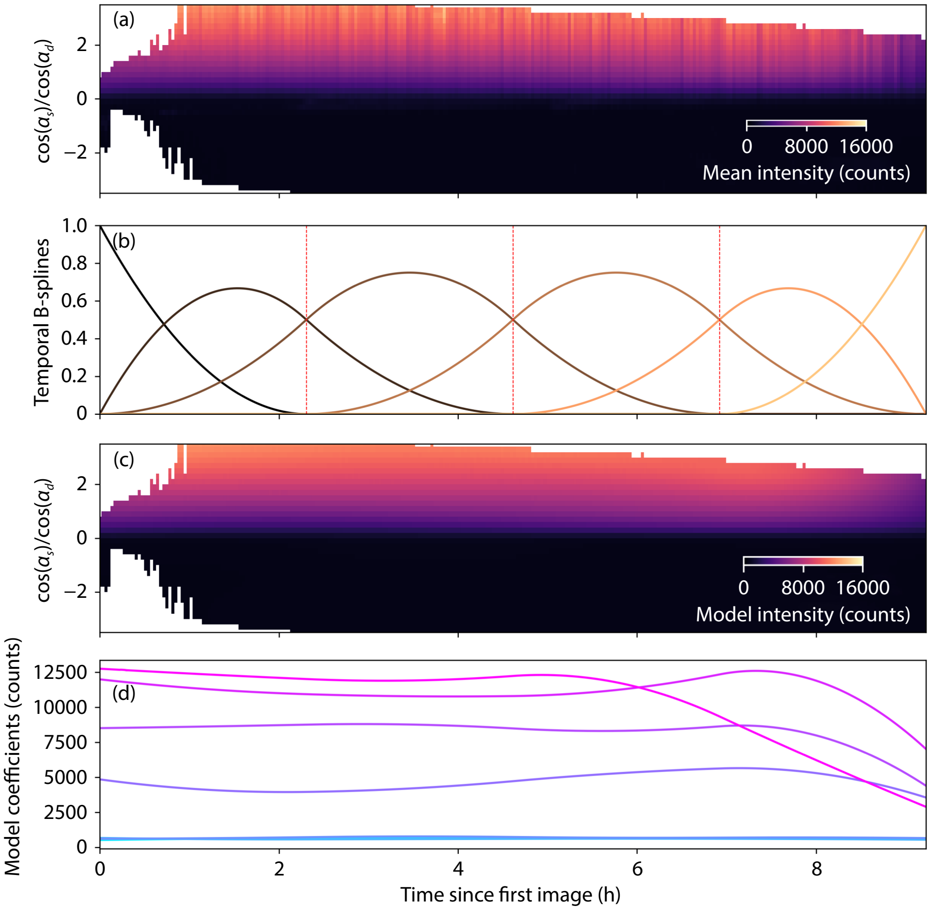

Figure 4. (a) Temporal evolution of binned mean intensities observed by WIC. The time is relative to the first image of the event (07:24:12 on 28 August 2000). (b) Temporal B-spline functions used to model the background. The vertical red lines indicate the locations of interior knot points. (c) Temporal evolution of the BS model after the final iteration. (d) Temporal evolution of the model coefficients, where the colors of each line correspond to the spatial B-splines in Figure 3.

display WIC, SI12, and SI13. From the left, the columns display the original image projected on Earth assuming a height of 130 km, the model, the corrected image and the weights after the final iteration. It is clear that subtracting the model from the observed intensities successfully removes most of the background and that auroral pixels are successfully deselected as outliers.

3.2 Residual Background Model

As is evident from Figure 5, a systematic residual background can be present in the B-spline corrected images. This can be related to real differences in the non-aurora emissions, due to, for instance, dawn–dusk asymmetries in the composition of the upper atmosphere following active periods. Instrumental effects, stray sunlight entering the detector, errors in the viewing angle correction, and/or errors in the geolocation of the images can also contribute to a systematic residual background.

We model this residual background intensity by using a spherical harmonic (SH) model:

$$I_{\mathrm{sh}}(\theta_g,\phi_g,t)=\sum_{n=0}^{N}\sum_{m=0}^{n}\left[g_n^m(t)\cos(m\phi_g)+h_n^m(t)\sin(m\phi_g)\right]P_n^m(\cos\theta_g). \quad (9)$$

Here n and m are the order and degree of the SH model, respectively. The ϕ_g is the longitude relative to the geographic longitude of the subsolar point, whereas θ_g is the geographic colatitude. The coefficients

$$g_n^m(t)=\sum_{l=1}^{L}g_{nl}^m B_l(t)\text{ and }h_n^m(t)=\sum_{l=1}^{L}h_{nl}^m B_l(t)$$

are the amplitudes of the surface waves, where the B-spline $B_l(t)$ allows for temporal variations. We have used the same degree and knot locations as the BS model (Figure 4b). The goal is to identify the model coefficients that best describe the residual background intensity $\boldsymbol{d}_r$ via the forward problem:

$$\boldsymbol{d}_r=\boldsymbol{G}_{\mathrm{sh}}\boldsymbol{m}_{\mathrm{sh}}. \quad (10)$$

To make the noise approximately white, we divide each row of both $\boldsymbol{d}_r$ and $\boldsymbol{G}_{\mathrm{sh}}$ by the corresponding σ obtained in the BS model. To avoid fitting the aurora, we use only low-order terms (N = 4). Because we model only one hemisphere, we do not need terms that describe interhemispheric asymmetries; and therefore, we consider only terms where $n-m$ is even. As with the BS model, the least-squares solution,

$$\boldsymbol{m}_{\mathrm{sh}}=(\boldsymbol{G}_{\mathrm{sh}}^{\mathrm{T}}\boldsymbol{W}\boldsymbol{G}_{\mathrm{sh}}+\lambda^2\boldsymbol{I})^{-1}\boldsymbol{G}_{\mathrm{sh}}^{\mathrm{T}}\boldsymbol{W}\boldsymbol{d}_r, \quad (11)$$

is used to find $\boldsymbol{m}_{\mathrm{sh}}$. Again, the diagonal matrix $\boldsymbol{W}=\boldsymbol{W}_c\boldsymbol{W}_t$ represents the weight of each observation. The data coverage part $\boldsymbol{W}_c$ is

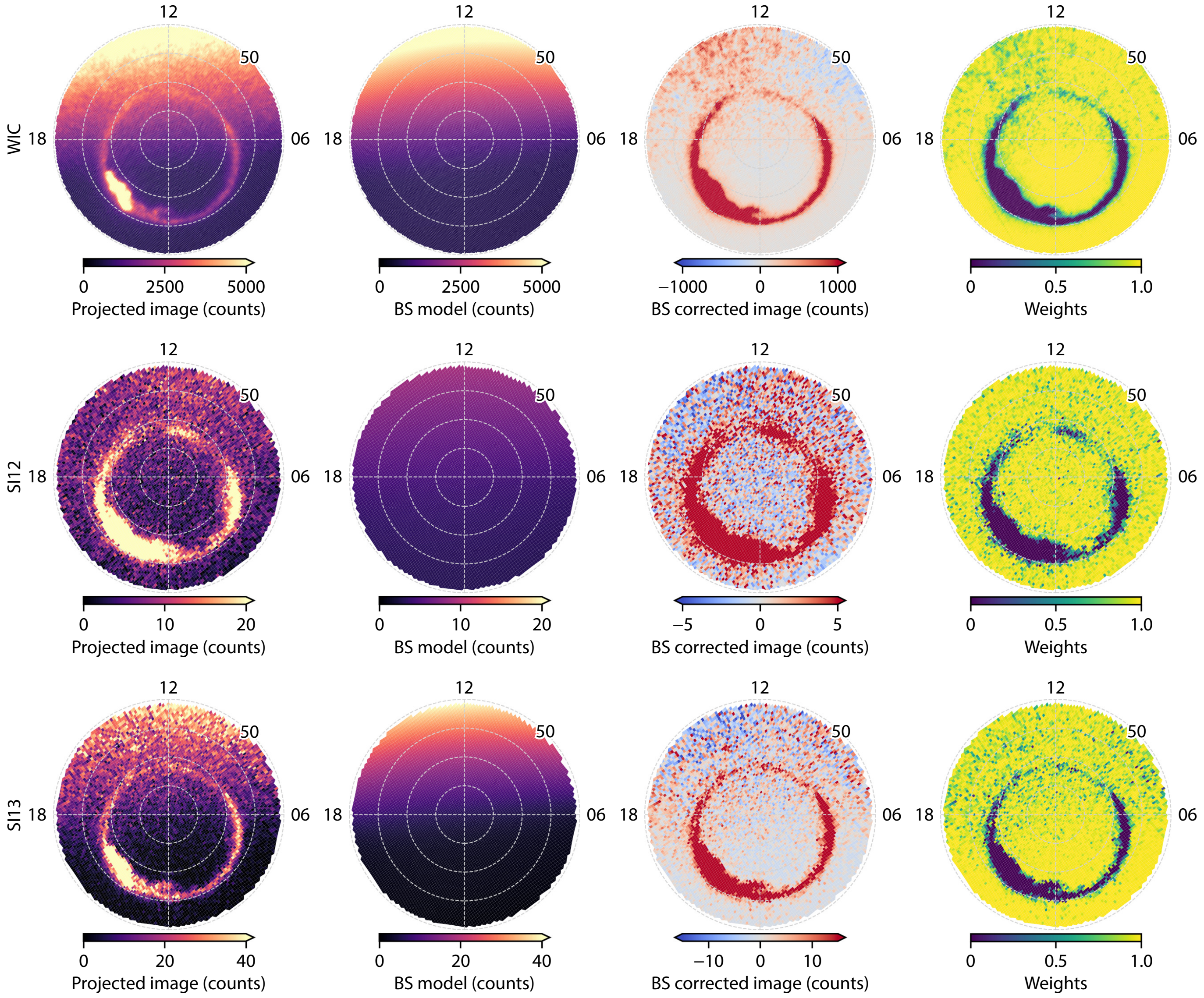

Figure 5. BS model applied to WIC (top), SI12 (middle) and SI13 (bottom) images obtained at 09:40:57 on 28 August 2000. From left to right, the columns display the original images projected on Earth, the BS models, the BS corrected images, and the weights after the final iteration.

determined as the inverse of the number of observations in each cell of an equal area grid, and $\mathbf{W}_t$ is the iteratively updated Tukey weights. The weights from the final iteration of the BS model are used in the first iteration of the SH model. On the basis of an *L*-curve analysis, we use λ values of 0.0001, 10, and 10 for the WIC, SI12, and SI13 images, respectively. As with the BS model, the SH model is updated until the model 2-norm converges.

The SH model applied to the images obtained at 09:40:57 UT on 28 August 2000 is displayed in Figure 6, in the same format as Figure 5. Especially in the WIC image, it is clear that the SH model captures the systematic dawn–dusk differences present in the BS corrected image. The SH corrected images thus have a more even background compared to the BS corrected images with no SH correction applied.

4. Discussion and Conclusions

In the foregoing sections, we have described a data-driven method to remove non-auroral emissions from global FUV images. The method is implemented in Python and is publicly available (Ohma et al., 2022a). The method has several advantages: It combines many images in two inversions while still allowing for (slow) temporal variations, which ensures robust statistics because of the abundance of data points used when constructing the models. This means that the model is also reliable when only a fraction of the auroral zone is observed because the conjunction of many images provides a global view. This can be seen in the first hour of Figure 4, where the modeled intensity matches the mean observed intensities despite the small region covered. Furthermore, the SH model captures potential dawn–dusk asymmetries in the background emissions, which could be critical during active periods. The method is highly flexible, and it is straightforward to adjust the location of knots and the order of both the spatial and temporal B-splines and to adjust the order and degree of the SH model. The final model is smooth everywhere (including across the terminator), and the iterative deselection of

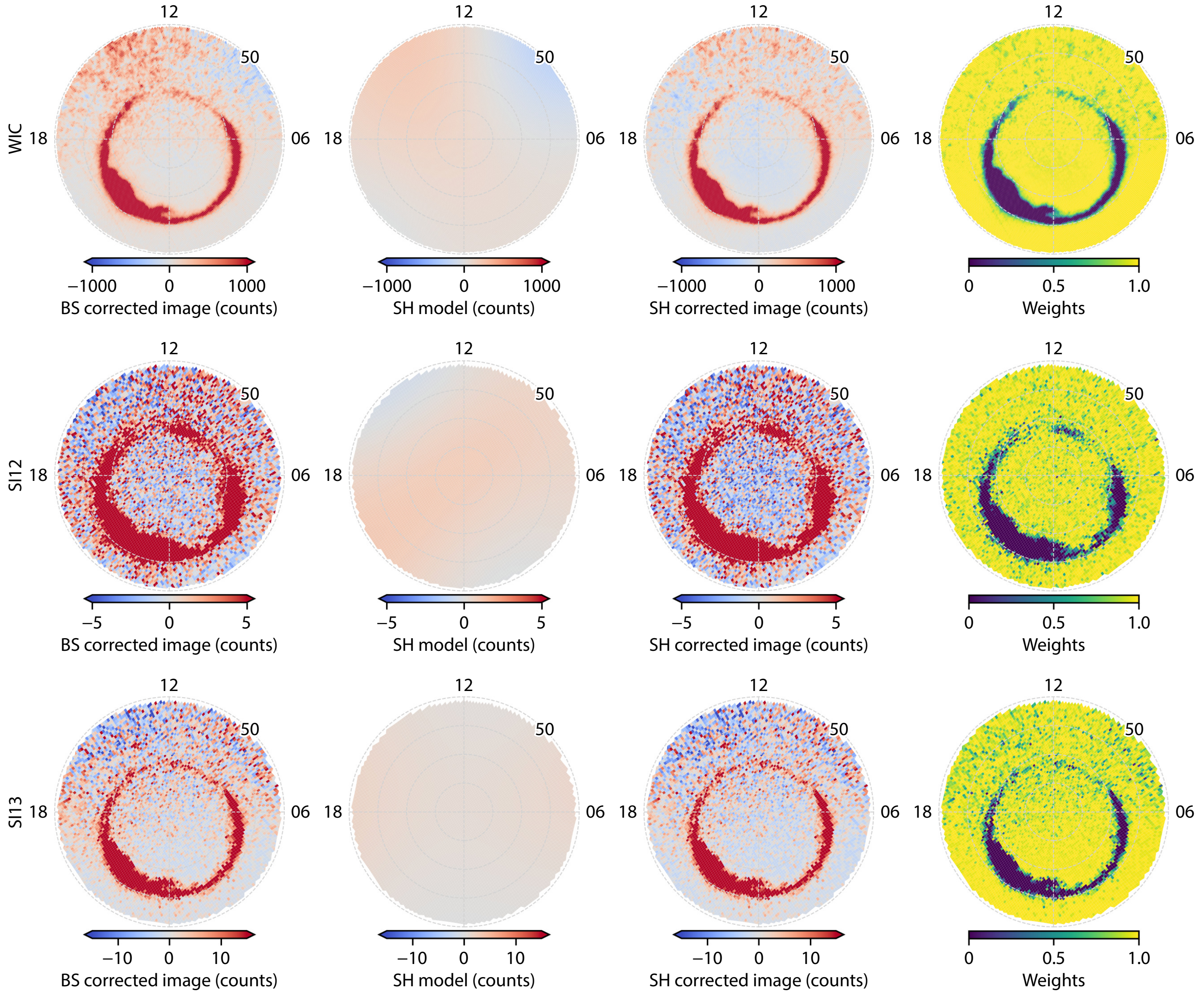

Figure 6. SH model applied to WIC (top), SI12 (middle), and SI13 (bottom) images obtained at 09:40:57 on 28 August 2000. From left to right, the columns display the BS corrected images, the SH models, the SH corrected images, and the weights after the final iteration.

outliers, such as aurora, means that we do not have to presume the location of the auroral oval.

Because we use B-splines to model the main dayglow signal, we do not presuppose the location of the terminator or the functional form of the dayglow relative to the solar zenith angle. We do, however, assume that the correction $1/\cos\alpha_d$ correctly accounts for the viewing geometry. Because this term goes to infinity at 90°, only the part of images below some upper limit should be used (e.g., between 70° and 80°). The geolocation is also very uncertain for large viewing angles. For imagers that observe optically thick emission lines, such as the Visible Imaging System Earth camera on Polar, no viewing angle correction should be applied. By correcting for the viewing angle, we map two-dimensional images to a single dimension, which we then model based on B-splines. The presence of large-scale residual features in the BS corrected images indicates that this mapping is not perfect. We have therefore introduced a second inversion based on spherical harmonics, in which we consider the full two-dimensional nature of the images, which reduces such large-scale residuals. In the presented event, the SH model is up to 10% of the BS model in the sunlit hemisphere, depending on the camera and location. The SH model intensities are weak in SI12 and SI13 but are comparable to the intensity of the dayside aurora in WIC. This should not be regarded as a general result because the magnitude of the SH model varies and the dayside aurora can be weak or even absent in other events. In a future project, we will consider the full two-dimensional problem (three-dimensional when considering the temporal dimension) by using B-splines defined on a sphere (Schumaker and Traas, 1991). If successful, the full dayglow can be modeled in a single inversion.

As is evident from Figure 4, there are rapid fluctuations in the observed intensities with time. By design, the background model does not capture such rapid changes. It is possible to pick up these fluctuations by applying the described method on individual images, similar to other dayglow fitting schemes used before (e.g., Lummerzheim et al., 1997; Li X et al., 2004; Laundal and Østgaard, 2009; Reistad et al., 2014). However, unless the fit is consistent for every image and the fluctuations are purely caused by differences in the baseline of the images, it is not possible to separate whether differences between two images are a result of differences in the signal or differences in the background detection. By enforcing only slow variations, we ensure that any rapid change is due to changes in the signal alone. This will occasionally lead to more residual background in the corrected images, but also a more robust model and easier interpretation when considering temporal changes.

In the BS model, we model σ as a function of $I_{\rm bs}$ to account for heteroskedasticity. We also divide by this quantity in the SH model to normalize the noise. An alternative way to account for heteroskedasticity is to perform a variance-stabilizing transformation. A suitable transformation can be found empirically by, for example, finding the best power transformation using the Box–Cox test (Box and Cox, 1964). If the functional form between the variance and the mean is known or can be reasonably assumed, the transformation providing homoskedasticity is proportional to $\int {\rm d}\mu/\sqrt{h(\mu)}$, where $h(\mu)$ is the function relating the mean μ to the variance (Bartlett, 1947). If the spread is simply proportional to the signal (relative error), this yields a logarithmic transformation. This transformation actually performs well when applied to WIC, but not when applied to SI12 and SI13. However, if there is both an absolute and a relative spread, as we assumed in Equation (8), the appropriate transformation becomes proportional to $\sinh(ds_d/\sigma_d)$, where d is the observed intensity. This means that both s_d and σ_d must be known a priori.

For SI12 and SI13, there is an additional instrumental effect to consider: the two detectors have a low dynamical range, which means that the observed intensities are quasi-discrete. The separation between measured intensity levels is equal in linear space, but any transformation will break this. For instance, a logarithmic transformation will lead to a large separation between the discrete levels for low intensities and a small separation between the discrete levels for high intensities, making it hard for the model to converge.

The background-corrected images contain many pixels with negative intensity (Figures 5 and 6) caused by spread in the original signal. Because negative auroral emissions have no physical meaning, they should be interpreted as regions without such emissions (zero intensity). However, if images are binned or fitted as part of a quantitative analysis, negative intensities should be included to avoid overestimation of the binned or fitted intensities.

The method outlined in this text can be applied to both previous and future missions with little or no adjustments to the algorithm. It can be used to remove background emissions from the auroral emissions in order to more easily examine the auroral topology, intensity, and dynamic evolution. The combined BS and SH models also provide a smooth representation of the dayglow emissions, which can be used to infer the column density of O/N_2 when applied to appropriate FUV emission lines (e.g., Meier, 1991, 2021). We hope the presented method can be a useful tool when analyzing large-scale FUV images, for example, for the upcoming SMILE mission, which also will have a camera in the LBH range.

Acknowledgments

This work was supported by the Research Council of Norway under contracts 223252/F50 and 300844/F50 and by the Trond Mohn Foundation. We thank S. B. Mende and the IMAGE FUV team at the Space Sciences Laboratory at UC Berkeley for the IMAGE FUV data. The original images can be accessed at https://spdf.gsfc.nasa.gov/pub/data/image/fuv/ and were processed using the FUVIEW3 software (http://sprg.ssl.berkeley.edu/image/).

References

Acuña, M. H., Ogilvie, K. W., Baker, D. N., Curtis, S. A., Fairfield, D. H., and Mish, W. H. (1995). The global geospace science program and its investigations. *Space Sci. Rev.*, *71*(1), 5–21. https://doi.org/10.1007/BF00751323

Anger, C. D., Fancott, T., McNally, J., and Kerr, H. S. (1973). ISIS-Ⅱ scanning auroral photometer. *Appl. Opt.*, *12*(8), 1753–1766. https://doi.org/10.1364/AO.12.001753

Anger, C. D., Moshupi, M. C., Wallis, D. D., Murphree, J. S., Brace, L. H., and Shepherd, G. G. (1978). Detached auroral arcs in the trough region. *J. Geophys. Res.: Space Phys.*, *83*(A6), 2683–2689. https://doi.org/10.1029/JA083iA06p02683

Anger, C. D., Babey, S. K., Broadfoot, A. L., Brown, R. G., Cogger, L. L., Gattinger, R., Haslett, J. W., King, R. A., McEwen, D. J., ... Jones, A. V. (1987). An ultraviolet auroral imager for the Viking spacecraft. *Geophys. Res. Lett.*, *14*(4), 387–390. https://doi.org/10.1029/GL014i004p00387

Bartlett, M. S. (1947). The use of transformations. *Biometrics*, *3*(1), 39–52. https://doi.org/10.2307/3001536

Beaton, A. E., and Tukey, J. W. (1974). The fitting of power series, meaning polynomials, illustrated on band-spectroscopic data. *Technometrics*, *16*(2), 147–185. https://doi.org/10.2307/1267936

Box, G. E. P., and Cox, D. R. (1964). An analysis of transformations. *J. Roy. Stat. Soc.: Ser. B* (*Methodol.*), *26*(2), 211–243. https://doi.org/10.1111/j.2517-6161.1964.tb00553.x

Brekke, A., and Moen, J. (1993). Observations of high latitude ionospheric conductances. *J. Atmos. Terr. Phys.*, *55*(11-12), 1493–1512. https://doi.org/10.1016/0021-9169(93)90126-J

Burch, J. L. (2000). IMAGE mission overview. *Space Sci. Rev.*, *91*(1-2), 1–14. https://doi.org/10.1023/A:1005245323115

Burch, J. L., Lewis, W. S., Immel, T. J., Anderson, P. C., Frey, H. U., Fuselier, S. A., Gérard, J. C., Mende, S. B., Mitchell, D. G., and Thomsen, M. F. (2002). Interplanetary magnetic field control of afternoon-sector detached proton auroral arcs. *J. Geophys. Res.: Space Phys.*, *107*(A9), 1251. https://doi.org/10.1029/2001JA007554

Carbary, J. F., Sotirelis, T., Newell, P. T., and Meng, C. I. (2003). Auroral boundary correlations between UVI and DMSP. *J. Geophys. Res.: Space Phys.*, *108*(A1), 1018. https://doi.org/10.1029/2002JA009378

Christensen, A. B., Paxton, L. J., Avery, S., Craven, J., Crowley, G., Humm, D. C., Kil, H., Meier, R. R., Meng, C. I., ... Zhang, Y. (2003). Initial observations with the Global Ultraviolet Imager (GUVI) in the NASA TIMED satellite mission. *J. Geophys. Res.: Space Phys.*, *108*(A12), 1451. https://doi.org/10.1029/2003JA009918

Cogger, L. L., Murphree, J. S., Ismail, S., and Anger, C. D. (1977). Characteristics of dayside 5577Å and 3914Å aurora. *Geophys. Res. Lett.*, *4*(10), 413–416. https://doi.org/10.1029/GL004i010p00413

Craven, J. D., Nicholas, A. C., Frank, L. A., Strickland, D. J., and Immel, T. J. (1994). Variations in the FUV dayglow after intense auroral activity. *Geophys. Res. Lett.*, *21*(25), 2793–2796. https://doi.org/10.1029/94GL02458

de Boor, C. (2001). *A Practical Guide to Splines*. New York: Springer.

Elphinstone, R. D., Hearn, D. J., Murphree, J. S., Cogger, L. L., Johnson, M. L., and Vo, H. B. (1993). Some UV dayside auroral morphologies. In R. L. Lysak (Ed.), *Auroral Plasma Dynamics* (pp. 31-45). Washington: American Geophysical Union.

Feldstein, Y. I. (1964). Auroral morphology, I. The location of the auroral zone.

Tellus, *16*(2), 252–257. https://doi.org/10.1111/j.2153-3490.1964.tb00163.x

Frank, L. A., Craven, J. D., Ackerson, K. L., English, M. R., Eather, R. H., and Carovillano, R. L. (1981). Global auroral imaging instrumentation for the Dynamics Explorer mission. *Space Sci. Instrum.*, *5*, 369–393.

Frank, L. A., Craven, J. D., Gurnett, D. A., Shawhan, S. D., Weimer, D. R., Burch, J. L., Winningham, J. D., Chappell, C. R., Waite, J. H., ... Shelley, E. G. (1986). The theta aurora. *J. Geophys. Res.*: *Space Phys.*, *91*(A3), 3177–3224. https://doi.org/10.1029/JA091iA03p03177

Frank, L. A., and Craven, J. D. (1988). Imaging results from Dynamics Explorer 1. *Rev. Geophys.*, *26*(2), 249–283. https://doi.org/10.1029/RG026i002p00249

Frank, L. A., Sigwarth, J. B., Craven, J. D., Cravens, J. P., Dolan, J. S., Dvorsky, M. R., Hardebeck, P. K., Harvey, J. D., and Muller, D. W. (1995). The visible imaging system (VIS) for the polar spacecraft. *Space Sci. Rev.*, *71*(1-4), 297–328. https://doi.org/10.1007/BF00751334

Frey, H. U., Immel, T. J., Lu, G., Bonnell, J., Fuselier, S. A., Mende, S. B., Hubert, B., Østgaard, N., and Le, G. (2003). Properties of localized, high latitude, dayside aurora. *J. Geophys. Res.*: *Space Phys.*, *108*(A4), 8008. https://doi.org/10.1029/2002JA009332

Frey, H. U., Mende, S. B., Immel, T. J., Gérard, J. C., Hubert, B., Habraken, S., Spann, J., Gladstone, G. R., Bisikalo, D. V., and Shematovich, V. I. (2003). Summary of quantitative interpretation of IMAGE far ultraviolet auroral data. *Space Sci. Rev.*, *109*(1-4), 255–283. https://doi.org/10.1023/B:SPAC.0000007521.39348.a5

Germany, G. A., Torr, D. G., Richards, P. G., Torr, M. R., and John, S. (1994a). Determination of ionospheric conductivities from FUV auroral emissions. *J. Geophys. Res.*: *Space Phys.*, *99*(A12), 23297–23305. https://doi.org/10.1029/94JA02038

Germany, G. A., Torr, M. R., Torr, D. G., and Richards, P. G. (1994b). Use of FUV auroral emissions as diagnostic indicators. *J. Geophys. Res.*: *Space Phys.*, *99*(A1), 383–388. https://doi.org/10.1029/93JA02357

Hansen, P. C. (1992). Analysis of discrete ill-posed problems by means of the L-curve. *SIAM Rev.*, *34*(4), 561–580. https://doi.org/10.1137/1034115

Hirao, K., and Itoh, T. (1978). Scientific satellite KYOKKO (EXOS-A). *Solar Terr. Environ. Res. Japan*, *2*, 148–152.

Huber, P. J. (1964). Robust estimation of a location parameter. *Ann. Math. Stat.*, *35*(1), 73–101. https://doi.org/10.1214/aoms/1177703732

Immel, T. J., Craven, J. D., and Nicholas, A. C. (2000). An empirical model of the OI FUV dayglow from DE-1 images. *J. Atmos. Solar-Terr. Phys.*, *62*(1), 47–64. https://doi.org/10.1016/S1364-6826(99)00082-6

Immel, T. J., Mende, S. B., Frey, H. U., Peticolas, L. M., Carlson, C. W., Gérard, J. C., Hubert, B., Fuselier, S. A., and Burch, J. L. (2002). Precipitation of auroral protons in detached arcs. *Geophys. Res. Lett.*, *29*(11), 1519. https://doi.org/10.1029/2001GL013847

Kamide, Y., Craven, J. D., Frank, L. A., Ahn, B. H., and Akasofu, S. I. (1986). Modeling substorm current systems using conductivity distributions inferred from DE auroral images. *J. Geophys. Res.*: *Space Phys.*, *91*(A10), 11235–11256. https://doi.org/10.1029/JA091iA10p11235

Kaneda, E., Takagi, M., and Niwa, N. (1977). Vacuum ultraviolet aurora television camera. In *Proceedings of the 12th International Symposium on Space Technology and Science* (pp. 233-238). Tokyo, Japan: University of Tokyo.

Laundal, K. M., and Østgaard, N. (2009). Asymmetric auroral intensities in the Earth's Northern and Southern hemispheres. *Nature*, *460*(7254), 491–493. https://doi.org/10.1038/nature08154

Laundal, K. M., Østgaard, N., Frey, H. U., and Weygand, J. M. (2010a). Seasonal and interplanetary magnetic field–dependent polar cap contraction during substorm expansion phase. *J. Geophys. Res.*: *Space Phys.*, *115*(A11), A11224. https://doi.org/10.1029/2010JA015910

Laundal, K. M., Østgaard, N., Snekvik, K., and Frey, H. U. (2010b). Interhemispheric observations of emerging polar cap asymmetries. *J. Geophys. Res.*: *Space Phys.*, *115*(A7), A07230. https://doi.org/10.1029/2009JA015160

Li, X., Ramachandran, R., Movva, S., Graves, S., Germany, G., Lyatsky, W., and Tan, A. (2004). Dayglow removal from FUV auroral images. In *Proceedings of 2004 IEEE International Geoscience and Remote Sensing Symposium* (pp. 3774-3777). Anchorage, USA: IEEE.

Liou, K., Newell, P. T., Meng, C. I., Brittnacher, M., and Parks, G. (1997). Synoptic auroral distribution: a survey using Polar ultraviolet imagery. *J. Geophys. Res.*: *Space Phys.*, *102*(A12), 27197–27205. https://doi.org/10.1029/97JA02638

Longden, N., Chisham, G., Freeman, M. P., Abel, G. A., and Sotirelis, T. (2010). Estimating the location of the open-closed magnetic field line boundary from auroral images. *Ann. Geophys.*, *28*(9), 1659–1678. https://doi.org/10.5194/angeo-28-1659-2010

Lui, A. T. Y., Anger, C. D., Venkatesan, D., Sawchuk, W., and Akasofu, S. I. (1975). The topology of the auroral oval as seen by the Isis 2 scanning auroral photometer. *J. Geophys. Res.*, *80*(13), 1795–1804. https://doi.org/10.1029/JA080i013p01795

Lummerzheim, D., Rees, M. H., Craven, J. D., and Frank, L. A. (1991). Ionospheric conductances derived from DE-1 auroral images. *J. Atmos. Terr. Phys.*, *53*(3-4), 281–292. https://doi.org/10.1016/0021-9169(91)90112-K

Lummerzheim, D., Brittnacher, M., Evans, D., Germany, G. A., Parks, G. K., Rees, M. H., and Spann, J. F. (1997). High time resolution study of the hemispheric power carried by energetic electrons into the ionosphere during the May 19/20, 1996 auroral activity. *Geophys. Res. Lett.*, *24*(8), 987–990. https://doi.org/10.1029/96GL03828

Meier, R. R. (1991). Ultraviolet spectroscopy and remote sensing of the upper atmosphere. *Space Sci. Rev.*, *58*(1), 1–185. https://doi.org/10.1007/BF01206000

Meier, R. R. (2021). The thermospheric column O/N_2 ratio. *J. Geophys. Res.*: *Space Phys.*, *126*(3), e2020JA029059. https://doi.org/10.1029/2020JA029059

Mende, S. B., Heetderks, H., Frey, H. U., Lampton, M., Geller, S. P., Abiad, R., Siegmund, O. H. W., Tremsin, A. S., Spann, J., ... Trondsen, T. (2000a). Far ultraviolet imaging from the IMAGE spacecraft. 2. Wideband FUV imaging. *Space Sci. Rev.*, *91*(1-2), 271–285. https://doi.org/10.1023/A:1005227915363

Mende, S. B., Heetderks, H., Frey, H. U., Lampton, M., Geller, S. P., Habraken, S., Renotte, E., Jamar, C., Rochus, P., ... Cogger, L. (2000b). Far ultraviolet imaging from the IMAGE spacecraft. 1. System design. *Space Sci. Rev.*, *91*(1-2), 243–270. https://doi.org/10.1023/A:1005271728567

Mende, S. B., Heetderks, H., Frey, H. U., Stock, J. M., Lampton, M., Geller, S. P., Abiad, R., Siegmund, O. H. W., Habraken, S., ... Lauche, H. (2000c). Far ultraviolet imaging from the IMAGE spacecraft. 3. Spectral imaging of Lyman-α and OI 135.6 nm. *Space Sci. Rev.*, *91*(1-2), 287–318. https://doi.org/10.1023/A:1005292301251

Murphree, J. S., Elphinstone, R. D., Hearn, D., and Cogger, L. L. (1990). Large-scale high-latitude dayside auroral emissions. *J. Geophys. Res.*: *Space Phys.*, *95*(A3), 2345–2354. https://doi.org/10.1029/JA095iA03p02345

Nicholas, A. C., Craven, J. D., and Frank, L. A. (1997). A survey of large-scale variations in thermospheric oxygen column density with magnetic activity as inferred from observations of the FUV dayglow. *J. Geophys. Res.*: *Space Phys.*, *102*(A3), 4493–4510. https://doi.org/10.1029/96JA03464

Oguti, T., Kaneda, E., Ejiri, M., Sasaki, S., Kadokura, A., Yamamoto, T., Hayashi, K., Fujii, R., and Makita, K. (1990). Studies of aurora dynamics by Aurora-TV on the Akebono (EXOS-D) satellite. *J. Geomagn. Geoelec.*, *42*(4), 555–564. https://doi.org/10.5636/jgg.42.555

Ohma, A., Østgaard, N., Reistad, J. P., Tenfjord, P., Laundal, K. M., Snekvik, K., Haaland, S. E., and Fillingim, M. O. (2018). Evolution of asymmetrically displaced footpoints during substorms. *J. Geophys. Res.*: *Space Phys.*, *123*(12), 10030–10063. https://doi.org/10.1029/2018JA025869

Ohma, A., Madelaire, M., Laundal, K. M., Reistad, J. P., and Walker, S. J. (2022a). Aohma/fuvpy: fuvpy (v1.0.1). Zenodo.

Ohma, A., Madelaire, M., Laundal, K. M., Reistad, J. P., and Walker, S. J. (2022b). IMAGE FUV data from 2000-08-28 07: 24: 12 to 2000-08-28 16: 37: 46 (v1.0.0). Zenodo.

Østgaard, N., Mende, S. B., Frey, H. U., Frank, L. A., and Sigwarth, J. B. (2003). Observations of non-conjugate theta aurora. *Geophys. Res. Lett.*, *30*(21), 2125. https://doi.org/10.1029/2003GL017914

Østgaard, N., Humberset, B. K., and Laundal, K. M. (2011). Evolution of auroral asymmetries in the conjugate hemispheres during two substorms. *Geophys. Res. Lett.*, *38*(3), L03101. https://doi.org/10.1029/2010GL046057

Østgaard, N., Reistad, J. P., Tenfjord, P., Laundal, K. M., Rexer, T., Haaland, S. E., Snekvik, K., Hesse, M., Milan, S. E., and Ohma, A. (2018). The asymmetric geospace as displayed during the geomagnetic storm on 17 August 2001. *Ann. Geophys.*, *36*(6), 1577–1596. https://doi.org/10.5194/angeo-36-1577-2018

Paxton, L. J., Meng, C. I., Fountain, G. H., Ogorzalek, B. S., Darlington, E. H., Gary, S. A., Goldsten, J. O., Kusnierkiewicz, D. Y., Lee, S. C., ... Smith, B. E. (1992). Special sensor ultraviolet spectrographic imager: an instrument description. In *Proceedings of SPIE 1745*, *Instrumentation for Planetary and Terrestrial Atmospheric Remote Sensing* (pp. 2-15). San Diego, United States: SPIE.

Paxton, L. J., Christensen, A. B., Humm, D. C., Ogorzalek, B. S., Pardoe, C. T., Morrison, D., Weiss, M. B., Crain, W., Lew, P. H., ... Meng, C. I. (1999). Global ultraviolet imager (GUVI): measuring composition and energy inputs for the NASA Thermosphere Ionosphere Mesosphere Energetics and Dynamics (TIMED) mission. In *Proceedings of SPIE 3756*, *Optical Spectroscopic Techniques and Instrumentation for Atmospheric and Space Research III* (pp. 265-276). Denver, United States: SPIE.

Raab, W., Branduardi-Raymont, G., Wang, C., Dai, L., Donovan, E., Enno, G., Escoubet, P., Holland, A., Jing, L., ... Zheng, J. (2016). SMILE: a joint ESA/CAS mission to investigate the interaction between the solar wind and Earth's magnetosphere. In *Proceedings of SPIE 9905*, *Space Telescopes and Instrumentation 2016*: *Ultraviolet to Gamma Ray* (pp. 990502). Edinburgh, United Kingdom: SPIE.

Reistad, J. P., Østgaard, N., Laundal, K. M., and Oksavik, K. (2013). On the non-conjugacy of nightside aurora and their generator mechanisms. *J. Geophys. Res.*: *Space Phys.*, *118*(6), 3394–3406. https://doi.org/10.1002/jgra.50300

Reistad, J. P., Østgaard, N., Laundal, K. M., Haaland, S., Tenfjord, P., Snekvik, K., Oksavik, K., and Milan, S. E. (2014). Intensity asymmetries in the dusk sector of the poleward auroral oval due to IMF B_x. *J. Geophys. Res.*: *Space Phys.*, *119*(12), 9497–9507. https://doi.org/10.1002/2014JA020216

Reistad, J. P., Østgaard, N., Tenfjord, P., Laundal, K. M., Snekvik, K., Haaland, S., Milan, S. E., Oksavik, K., Frey, H. U., and Grocott, A. (2016). Dynamic effects of restoring footpoint symmetry on closed magnetic field lines. *J. Geophys. Res.*: *Space Phys.*, *121*(5), 3963–3977. https://doi.org/10.1002/2015JA022058

Schumaker, L. L., and Traas, C. (1991). Fitting scattered data on spherelike surfaces using tensor products of trigonometric and polynomial splines. *Numer. Math.*, *60*(1), 133–144. https://doi.org/10.1007/BF01385718

Sergeev, V. A., Sauvaud, J. A., Popescu, D., Kovrazhkin, R. A., Liou, K., Newell, P. T., Brittnacher, M., Parks, G., Nakamura, R., ... Reeves, G. D. (2000). Multiple-spacecraft observation of a narrow transient plasma jet in the Earth's plasma sheet. *Geophys. Res. Lett.*, *27*(6), 851–854. https://doi.org/10.1029/1999GL010729

Strickland, D. J., Bishop, J., Evans, J. S., Majeed, T., Shen, P. M., Cox, R. J., Link, R., and Huffman, R. E. (1999). Atmospheric Ultraviolet Radiance Integrated Code (AURIC): theory, software architecture, inputs, and selected results. *J. Quant. Spectrosc. Radiat. Transfer*, *62*(6), 689–742. https://doi.org/10.1016/S0022-4073(98)00098-3

Torr, M. R., Torr, D. G., Zukic, M., Johnson, R. B., Ajello, J., Banks, P., Clark, K., Cole, K., Keffer, C., ... Spann, J. (1995). A far ultraviolet imager for the international solar-terrestrial physics mission. *Space Sci. Rev.*, *71*(1-4), 329–383. https://doi.org/10.1007/BF00751335

Vestine, E. H. (1944). The geographic incidence of aurora and magnetic disturbance, northern hemisphere. *Terr. Magn. Atmos. Electr.*, *49*(2), 77–102. https://doi.org/10.1029/TE049i002p00077

Wang, L. M., Luan, X. L., Lei, J. H., and Dou, X. K. (2018). An empirical dayglow model for the lyman-birge-hopfield-long band derived from the polar ultraviolet imager data. *Space Wea.*, *16*(8), 1101–1113. https://doi.org/10.1029/2018SW001954

Zelenyi, L. M., Triska, P., and Petrukovich, A. A. (1997). INTERBALL—Dual probe and dual mission. *Adv. Space Res.*, *20*(4-5), 549–557. https://doi.org/10.1016/S0273-1177(97)00438-9

Zesta, E., Lyons, L. R., and Donovan, E. (2000). The auroral signature of earthward flow bursts observed in the magnetotail. *Geophys. Res. Lett.*, *27*(20), 3241–3244. https://doi.org/10.1029/2000GL000027

Zhang, Q. H., Zhang, Y. L., Wang, C., Oksavik, K., Lyons, L. R., Lockwood, M., Yang, H. G., Tang, B. B., Moen, J. I., ... Xia, L. D. (2021). A space hurricane over the Earth's polar ionosphere. *Nat. Commun.*, *12*(1), 1207. https://doi.org/10.1038/s41467-021-21459-y

Zhang, Y. L., Paxton, L. J., and Schaefer, R. (2022). Comments on "A new method to subtract dayglow for auroral observation of SSUSI in LBH ranges based on the improved AURIC" by Wang et al. (2021). *J. Atmos. Solar-Terr. Phys.*, *229*, 105833. https://doi.org/10.1016/j.jastp.2022.105833

Zhang, Y., and Paxton, L. J. (2008). An empirical Kp-dependent global auroral model based on TIMED/GUVI FUV data. *J. Atmos. Solar-Terr. Phys.*, *70*(8-9), 1231–1242. https://doi.org/10.1016/j.jastp.2008.03.008